



LJMU Research Online

Barnes, AT, Liu, J, Zhang, Q, Tan, JC, Bigiel, F, Caselli, P, Cosentino, G, Fontani, F, Henshaw, JD, Jiménez-Serra, I, Kalb, D-S, Law, CY, Longmore, SN, Parker, RJ, Pineda, JE, Sánchez-Monge, A, Lim, W and Wang, K

Mother of Dragons: A Massive, quiescent core in the dragon cloud (IRDC G028.37+00.07)

<http://researchonline.ljmu.ac.uk/id/eprint/19243/>

Article

Citation (please note it is advisable to refer to the publisher's version if you intend to cite from this work)

Barnes, AT, Liu, J, Zhang, Q, Tan, JC, Bigiel, F, Caselli, P, Cosentino, G, Fontani, F, Henshaw, JD, Jiménez-Serra, I, Kalb, D-S, Law, CY, Longmore, SN, Parker, RJ, Pineda, JE, Sánchez-Monge, A, Lim, W and Wang, K (2023) Mother of Dragons: A Massive, quiescent core in the dragon cloud (IRDC

LJMU has developed **LJMU Research Online** for users to access the research output of the University more effectively. Copyright © and Moral Rights for the papers on this site are retained by the individual authors and/or other copyright owners. Users may download and/or print one copy of any article(s) in LJMU Research Online to facilitate their private study or for non-commercial research. You may not engage in further distribution of the material or use it for any profit-making activities or any commercial gain.

The version presented here may differ from the published version or from the version of the record. Please see the repository URL above for details on accessing the published version and note that access may require a subscription.

For more information please contact researchonline@ljmu.ac.uk

<http://researchonline.ljmu.ac.uk/>

Mother of dragons

A massive, quiescent core in the dragon cloud (IRDC G028.37+00.07)

A. T. Barnes^{1,2}, J. Liu³, Q. Zhang⁴, J. C. Tan^{5,6}, F. Bigiel², P. Caselli⁷, G. Cosentino⁵, F. Fontani⁸, J. D. Henshaw^{9,10}, I. Jiménez-Serra¹¹, D.-S. Kalb¹⁰, C. Y. Law^{1,5}, S. N. Longmore⁹, R. J. Parker^{12,*}, J. E. Pineda⁷, A. Sánchez-Monge¹³, W. Lim¹⁴, and K. Wang¹⁵

¹ European Southern Observatory (ESO), Karl-Schwarzschild-Straße 2, 85748 Garching, Germany
e-mail: ashleybarnes.astro@gmail.com

² Argelander-Institut für Astronomie, Universität Bonn, Auf dem Hügel 71, 53121 Bonn, Germany

³ East Asian Observatory, 660 N. A'ohokū Place, University Park, Hilo, HI, USA

⁴ Center for Astrophysics | Harvard & Smithsonian, Cambridge, MA, USA

⁵ Dept. of Space, Earth and Environment, Chalmers University of Technology, SE-412 96 Gothenburg, Sweden

⁶ Department of Astronomy, University of Virginia, 530 McCormick Road, Charlottesville 22904-4325, USA

⁷ Max-Planck-Institut für extraterrestrische Physik, Giessenbachstrasse 1, 85748 Garching bei München, Germany

⁸ INAF Osservatorio Astrofisico di Arcetri, Largo E. Fermi 5, 50125 Florence, Italy

⁹ Astrophysics Research Institute, Liverpool John Moores University, 146 Brownlow Hill, Liverpool L3 5RF, UK

¹⁰ Max Planck Institute for Astronomy, Königstuhl 17, 69117 Heidelberg, Germany

¹¹ Centro de Astrobiología (CSIC/INTA), Instituto Nacional de Técnica Aeroespacial, 28850 Torrejón de Ardoz, Madrid, Spain

¹² Department of Physics and Astronomy, The University of Sheffield, Hicks Building, Hounsfield Road, Sheffield S3 7RH, UK

¹³ Observatorio Astronómico Nacional (OAN, IGN), Calle Alfonso XII 3, 28014 Madrid, Spain

¹⁴ IPAC, Mail Code 100-22, Caltech, 1200 E. California Boulevard, Pasadena, CA 91125, USA

¹⁵ Kavli Institute for Astronomy and Astrophysics, Peking University, 5 Yiheyuan Road, Haidian District, Beijing 100871, PR China

Received 12 December 2022 / Accepted 8 March 2023

ABSTRACT

Context. Core accretion models of massive star formation require the existence of massive, starless cores within molecular clouds. Yet, only a small number of candidates for such truly massive, monolithic cores are currently known.

Aims. Here we analyse a massive core in the well-studied infrared-dark cloud (IRDC) called the ‘dragon cloud’ (also known as G028.37+00.07 or ‘Cloud C’). This core (C2c1) sits at the end of a chain of a roughly equally spaced actively star-forming cores near the center of the IRDC.

Methods. We present new high-angular-resolution 1 mm ALMA dust continuum and molecular line observations of the massive core.

Results. The high-angular-resolution observations show that this region fragments into two cores, C2c1a and C2c1b, which retain significant background-subtracted masses of $23 M_{\odot}$ and $2 M_{\odot}$ ($31 M_{\odot}$ and $6 M_{\odot}$ without background subtraction), respectively. The cores do not appear to fragment further on the scales of our highest-angular-resolution images ($0.2''$, $0.005 \text{ pc} \sim 1000 \text{ AU}$). We find that these cores are very dense ($n_{\text{H}_2} > 10^6 \text{ cm}^{-3}$) and have only trans-sonic non-thermal motions ($\mathcal{M}_{\text{k}} \sim 1$). Together the mass, density, and internal motions imply a virial parameter of < 1 , which suggests the cores are gravitationally unstable, unless supported by strong magnetic fields with strengths of $\sim 1\text{--}10 \text{ mG}$. From CO line observations, we find that there is tentative evidence for a weak molecular outflow towards the lower-mass core, and yet the more massive core remains devoid of any star formation indicators.

Conclusions. We present evidence for the existence of a massive, pre-stellar core, which has implications for theories of massive star formation. This source warrants follow-up higher-angular-resolution observations to further assess its monolithic and pre-stellar nature.

Key words. stars: formation – stars: massive – ISM: structure – ISM: clouds

1. Introduction

Massive stars (i.e. with initial masses $> 8 M_{\odot}$) inject vast amounts of energy and momentum into the interstellar medium during and at the end of their relatively short lives, thus helping drive both local and galaxy-scale physical and chemical evolution (e.g. Krumholz et al. 2014). However, understanding how massive stars form remains one of the major unanswered questions in astrophysics (e.g. Tan et al. 2014).

One way to test different formation theories is to study the initial conditions of massive star formation. In particular, ‘core

accretion’ theories (e.g. McLaughlin & Pudritz 1997; McKee & Tan 2003) invoke the existence of massive, gravitationally bound pre-stellar cores as the initial condition. On the other hand, ‘competitive accretion’ theories and simulations (e.g. Bonnell et al. 2001; Wang et al. 2010; Padoan et al. 2020) do not involve such structures, but rather start with low-mass protostellar cores, some of which competitively accrete to form high-mass stars, being fed by global infall from the protocluster clump. Other authors have pointed out that the gas around massive protostars and star clusters often exhibits a hub-filament type morphology (e.g. Myers 2009); this has implications for how material is spatially and kinematically distributed around protostellar systems but in itself does not distinguish between the two basic scenarios.

* Royal Society Dorothy Hodgkin Fellow.

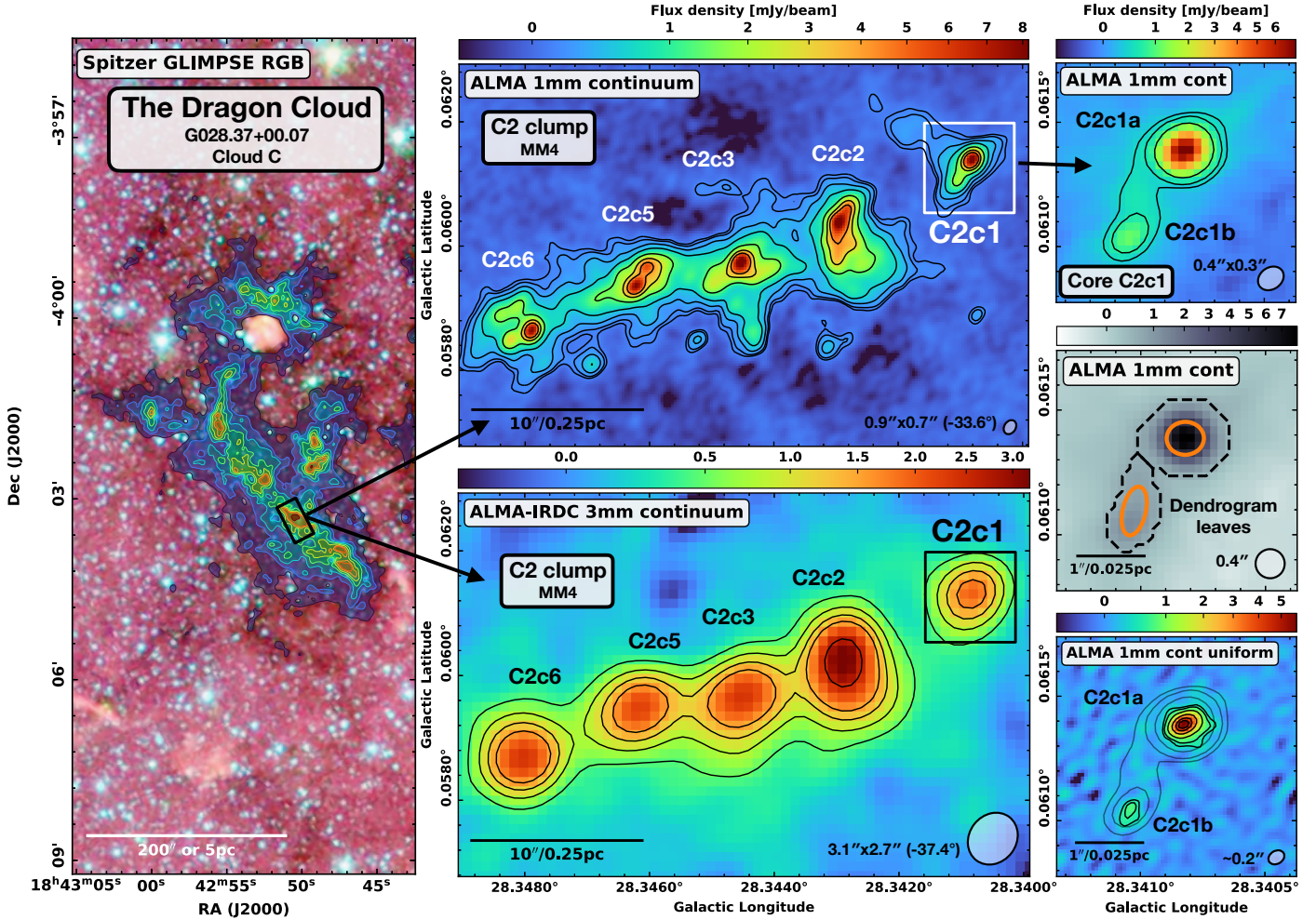


Fig. 1. Overview of the dragon cloud (also known as G028.37+00.07 or Cloud C), the C2 clump (also known as MM4), and the C2c1 core region. *Left:* Three-colour image of the Galactic plane in which the IRDC Cloud C can be seen as a strong dark extinction feature. In this image, red is 8 μm , green is 5.8 μm , and blue is 4.5 μm emission from the *Spitzer* GLIMPSE survey (Churchwell et al. 2009). Overlaid as coloured contours is the combined near- and mid-infrared extinction-derived dust mass surface density map, in levels of 0.1, 0.15, 0.2, 0.25, 0.3, 0.35, 0.375, and 0.45 g cm^{-2} (Kainulainen & Tan 2013). *Center top:* ALMA 1 mm dust continuum at 0.8'' resolution (Liu et al. 2020), overlaid with contours of 0.084, 0.14, 0.28, 0.56, 1.4, 2.8, and 4.2 mJy beam^{-1} . *Centre bottom:* ALMA-IRDC 3 mm dust continuum taken from ALMA-IRDC at 3'' resolution (Barnes et al. 2021), overlaid with contours of 0.49, 0.81, 1.13, 1.46, and 2.43 mJy beam^{-1} . *Right top:* Zoom in on the high-resolution 1 mm continuum image taken with only the longest baseline configuration, overlaid with contours of 0.4, 0.6, and 1.2 mJy beam^{-1} . *Right center:* ALMA 1 mm dust continuum with a circularised 0.4'' beam, which was used for the dendrogram analysis. The dashed black contours indicate the boundaries of the identified cores, whilst the orange ellipses show the intensity-weighted second moment along the two spatial dimensions within the contour (e.g. Rosolowsky et al. 2008). *Right bottom:* Same 1 mm observations imaged with a robust -2 (close to uniform) weighting scheme to maximise the resolution ($0.24'' \times 0.19''$, or ~ 0.05 pc), overlaid with contours of 0.4, 0.6, 1.2, 2.5, 4, and 5 mJy beam^{-1} (solid black line). Shown on the right of the ALMA observation panels is the beam size, and a scale bar is shown in the lower left of all panels.

Thus, identifying and characterising massive pre-stellar cores remains a primary way to distinguish between massive star formation scenarios. However, to date, only a handful of candidate massive pre-stellar cores have been identified. A non-exhaustive list of candidates and/or searches includes: Bontemps et al. (2010), Tan et al. (2013), Duarte-Cabral et al. (2013), Wang et al. (2014), Cyganowski et al. (2014), Sanhueza et al. (2017), Nony et al. (2018), Louvet et al. (2019), and Kong et al. (2018). Yet, despite these efforts, there are relatively few candidates of massive pre-stellar cores. It thus remains important to try to identify additional examples of massive pre-stellar cores.

Recently, a study of high-sensitivity 3 mm dust continuum and molecular line ALMA observations at $\sim 2''$ resolution identified a population of compact, massive cores that presented the potential birth sites of high-mass star formation (Barnes et al.

2021; Fontani et al. 2021). Out of this sample of 19 cores, one stood out as being a particularly strong monolithic core candidate. This core, known as C2c1 (called core 5 in Liu et al. 2020), is located within the ‘dragon cloud’ (also known as G028.37+00.07 and referred to as Cloud C by Butler & Tan 2009; see Wang 2015) at a distance of 5 kpc (Simon et al. 2006). Barnes et al. (2021) highlighted that this core does not fragment down to ~ 0.01 pc, and at this scale it still has more than enough mass to form a high-mass star (total mass of $40 M_{\odot}$; also see Wang et al. 2011; Zhang et al. 2015). Moreover, this source shows no signs of infrared point source emission (see our Fig. 1 and Sect. 6; Kong et al. 2019; Barnes et al. 2021). Broadband spectral line imaging shows that C2c1 is associated with very little molecular line emission (Zhang et al. 2015). It has only low levels of CO emission, indicating a CO depletion factor (fraction of

Table 1. Summary of the C2c1a and C2c1b core properties.

Property	C2c1a	C2c1b
Longitude (deg)	28.3408	28.3410
Latitude (deg)	0.0614	0.0611
r_{eff} (arcsec)	0.57	0.43
r_{eff} (pc)	0.014	0.010
r_{eff} (AU)	2827	2127
S_{ν} (no background sub.) (mJy)	12.89±1.29	2.43±0.24
S_{ν} (background sub.) (mJy)	9.65±0.97	0.64±0.06
T_{dust} (K)	10.4±3.0	10.4±3.0
M (no background sub.) (M_{\odot})	30.9±12.4	5.8±2.3
M (background sub.) (M_{\odot})	23.1±9.2	1.5±0.6
n_{H_2} (10^6 cm^{-3})	31.21±12.48	4.86±1.94
t_{ff} (yr)	5525±2762	14 000±7000
v_{LSR} (km s^{-1})	79.36±0.03	79.08±0.04
σ_{obs} (km s^{-1})	0.35±0.04	0.25±0.05
c_s (km s^{-1})	0.19±0.06	0.19±0.06
$\sigma_{\text{obs,corr}}$ (km s^{-1})	0.34±0.04	0.25±0.05
σ_{NT} (km s^{-1})	0.34±0.10	0.24±0.07
σ_{tot} (km s^{-1})	0.39±0.12	0.31±0.09
$M_s = \sigma_{\text{NT}}/c_s$	1.8±0.7	1.2±0.5
M_J (M_{\odot})	0.05±0.03	0.13±0.06
λ_J (AU)	733±366	1858±929
α_{vir}	0.10±0.05	0.74±0.37
$M_{\text{J,tot}}$ (M_{\odot})	0.42±0.21	0.52±0.26
B (mG)	10.0±5.0	1.0±0.5
B_{med} (mG)	14.4±7.2	4.3±2.2
Σ_{cl} (g cm^{-2})	0.62±0.25	0.62±0.25
$\sigma_{\text{c,vir}}$ (km s^{-1})	0.70±0.35	0.35±0.18
$\sigma_{\text{c,vir}}(B_{\text{med}})$ (km s^{-1})	0.26±0.13	0.14±0.07
$R_{\sigma} = \sigma_{\text{tot}}/\sigma_{\text{c,vir}}$	0.56±0.28	0.87±0.43
$R_{\sigma}(B_{\text{med}}) = \sigma_{\text{tot}}/\sigma_{\text{c,vir}}(B_{\text{med}})$	1.50±0.75	2.26±1.13

Notes. We outline how each of these properties is measured in Sects. 3, 4, and 5. The quoted T_{dust} values are taken from Wang et al. (2012). Note that all the properties listed here that are calculated with the mass use the values that include background subtraction.

CO molecules frozen out of the gas phase onto dust grains) of up to 10^3 at a scale of over 0.07 pc. In addition, the region also shows moderate N_2D^+ emission, highlighting an enhanced abundance of deuterated molecules, which is typically only seen towards the coldest and densest environments (with elevated CO freeze-out; see e.g. Kong et al. 2016; Barnes et al. 2016). Altogether, this is indicative of a pre-stellar nature for core C2c1 (Wang et al. 2011; Zhang et al. 2015; Kong et al. 2016, 2017; Liu et al. 2020) and makes it one of only a handful of potential monolithic massive core candidates.

Due to its location at the end of a string of cores near the centre of Cloud C, and its positioning at the edge of the primary beam response for most of the initial interferometric observations (e.g. Wang et al. 2011; Zhang et al. 2015; Kong et al. 2016, 2017), C2c1 has mostly eluded detailed study (e.g. Liu et al. 2020; Barnes et al. 2021). In this work, we make use of new high-resolution continuum and N_2D^+ observations (the latter a sensitive molecular line tracer of dense and cold gas) to study C2c1 in detail, in an effort to unveil its geometrical, chemical, and dynamical structure. The properties of C2c1 determined in this work are summarised in Table 1.

2. Observations

To investigate the dense gas properties within Cloud C, we collected several high-angular-resolution dust continuum and molecular line observations with ALMA. The data were taken as part of the project 2017.1.00793.S (see Liu et al. 2020 for the complete data reduction details and Liu et al., in prep.). In our analysis, we made use of the 1 mm continuum images with the observed longest baseline configuration, which provides a beam of $0.396'' \times 0.314''$ with a position angle of 55° , and a noise of $0.1 \text{ mJy beam}^{-1}$. The CO(2–1) cube (230.538 GHz rest frequency) also imaged with this configuration has a beam of $0.40'' \times 0.32''$ with a position angle of 60.8° , a spectral resolution of 0.16 km s^{-1} , and noise of $\sim 4 \text{ mJy beam}^{-1}$ per channel. For the N_2D^+ (3–2) cube (231.322 GHz rest frequency), we made use of the images that include both array configurations observed as part of project 2017.1.00793.S, as the smaller baselines were then needed to recover the lower brightness emission. They have a beam of $0.93'' \times 0.74''$ with a position angle of -3.4° , a spectral resolution of 0.16 km s^{-1} , and noise of 0.3 K per channel.

3. Fragmentation and mass distribution of C2c1

Figure 1 shows how the dust extinction and continuum emission (i.e. mass) distribution of the region changes from scales of several parsecs (cloud) down to 0.01 parsec (core). We see that the initially filamentary cloud (left panels) breaks down into regularly spaced cores within the MM4 ‘clump’ region (centre panels). The brightest cores within this region have been studied in detail (e.g. Zhang et al. 2009, 2015; Wang et al. 2008, 2011, 2012); they are found to be relatively massive but to already show signs of near-infrared emission and SiO and CO outflows – indicative of active star formation. The core C2c1 is seen at the end of this string of cores and appears to be somewhat disconnected in the extended envelope of millimetre-continuum emission that surrounds the main cores. A more detailed look at C2c1 (right panels) shows that it in fact breaks into two cores surrounded by a common envelope – denoted here as C2c1a and C2c1b (see also Zhang et al. 2015).

We characterised the mass fragmentation of this region using a dendrogram analysis (Rosolowsky et al. 2008), which was chosen to allow a direct comparison to other works that study our cloud sample (Henshaw et al. 2016, 2017; Liu et al. 2018; Barnes et al. 2021). We ran the dendrogram analysis using the continuum maps with a circularised $\sim 0.4''$ beam, which was corrected for the primary beam response. We note, however, that the primary beam correction has little effect on the total flux or flux distribution towards and around the core, as the full mosaic covers a much larger region (i.e. the right panels of Fig. 1 only show a zoomed-in view towards the core). The set of parameters that are used for the determination of the dendrogram structure is: $\text{MIN_VALUE} = 3\sigma = 0.22 \text{ mJy beam}^{-1}$ (the minimum intensity considered in the analysis); $\text{MIN_DELTA} = 3\sigma$ (the minimum spacing between isocontours); and $\text{MIN_PIX} = 1 \text{ beam area} \sim 12 \text{ pixels}$ (the minimum number of pixels contained within a structure). We found that the identified structure was robust against changes ($\pm 2\sigma$) in the dendrogram parameters; core C2c1a has a peak of $\sim 60\sigma$.

We find that the dendrogram analysis cleanly identifies both cores within the C2c1 region as ‘leaves’ – the highest level (smallest) structures in the dendrogram hierarchy. These cores are overlaid as dashed black contours on the continuum map shown in Fig. 1 (right centre panel). We find the effective radii ($r_{\text{eff}} = \sqrt{A/\pi}$, where A is the area enclosed within the

dendrogram boundary) of C2c1a and C2c1b to be $0.57''$ and $0.43''$, which, at the cloud kinematic distance (d) of 5 kpc (Simon et al. 2006), corresponds to 0.014 pc (2800 AU) and 0.010 pc (2100 AU), respectively.

The flux densities (S_ν) integrated within C2c1a and C2c1b are 12.9 and 2.4 mJy. After subtracting the background level, following the method outlined in Barnes et al. (2021), they are 9.7 and 0.6 mJy (75 and 25% of the flux before background subtraction). We made use of these flux values in the following mass estimation,

$$M = \frac{d^2 S_\nu R_{\text{gd}}}{\kappa_\nu B_\nu(T_{\text{dust}})}, \quad (1)$$

where $R_{\text{gd}} = 141$ is the ratio of the total dust mass (i.e. the gas plus the dust) over the refractory-component dust mass (assuming a typical interstellar composition of H, He, and metals; Draine 2011), $B_\nu(T)$ is the Planck function for a given temperature (T_{dust}) at a representative frequency of $\nu = 216.44$ GHz, and $\kappa_\nu = \kappa_0 (\nu/\nu_0)^\beta \approx 0.175 \text{ cm}^2 \text{ g}^{-1}$, when assuming the $\nu_0 = 230$ GHz, $\beta = 1.75$, and $\kappa_0 = 0.899 \text{ cm}^2 \text{ g}^{-1}$ obtained from Ossenkopf & Henning 1994 for a Mathis et al. (1977, i.e. MNR) size distribution with thin ice mantles after 10^5 yr of coagulation at a density of 10^6 cm^{-3} . Wang et al. (2012) used $2.8''$ NH_3 (1,1) and (2,2) observations from the Very Large Array (VLA) to obtain rotational temperatures of 9.2 K and 11.6 K towards C2c1a and C2c1b (also see Table 1 of Zhang et al. 2015). As the cores are not fully resolved in these VLA observations, we took the mean temperature of 10.4 K for T_{dust} in this analysis. When doing so, we calculated background-subtracted masses for C2c1a and C2c1b of $23.1 M_\odot$ and $1.5 M_\odot$ ($31 M_\odot$ and $6 M_\odot$ without the background subtraction).

The molecular hydrogen number density of each core was determined assuming a uniform density sphere,

$$n_{\text{H}_2} = \frac{M}{\frac{4}{3}\pi r_{\text{eff}}^3 \mu_{\text{H}_2} m_{\text{H}}}, \quad (2)$$

where $\mu_{\text{H}_2} = 2.8$ is the mean molecular weight per hydrogen molecule, and m_{H} is the mass of a hydrogen atom. We find n_{H_2} $31.2 \times 10^6 \text{ cm}^{-3}$ and $4.9 \times 10^6 \text{ cm}^{-3}$ for C2c1a and C2c1b. The corresponding local free-fall time is calculated as

$$t_{\text{ff}} = \left(\frac{\pi^2 r_{\text{eff}}^3}{8GM} \right)^{0.5} = \left(\frac{3\pi}{32G\mu_{\text{H}_2} m_{\text{H}} n_{\text{H}_2}} \right)^{0.5}, \quad (3)$$

where G is the gravitational constant. We find local free-fall times of 5500 and 14 000 yr for C2c1a and C2c1b, respectively.

Overall, these properties indicate that both cores, C2c1a and C2c1b, are dense, have very short free-fall times, and remain un-fragmented on scales of a few thousand AU. In particular, they highlight C2c1a as a strong candidate to form a massive star ($>8 M_\odot$). That said, there are several uncertainties in our calculations that are worth outlining. We assumed a typically $\sim 10\%$ uncertainty in the absolute flux scale of the ALMA observations, and, following Sanhueza et al. (2017), we assumed an uncertainty of $\sim 30\%$ dust opacity. These uncertainties in the dust opacity, dust emission fluxes, and a $\sim 30\%$ uncertainty on the distance propagate to give an uncertainty of 40–50% for the masses. Moreover, we note that choosing the average *Herschel*-derived dust temperature across the region of ~ 15 K (determined at much lower angular resolution; Barnes et al. 2021), and a lower $R_{\text{gd}} = 100$, gives background-subtracted masses of $9.5 M_\odot$ and

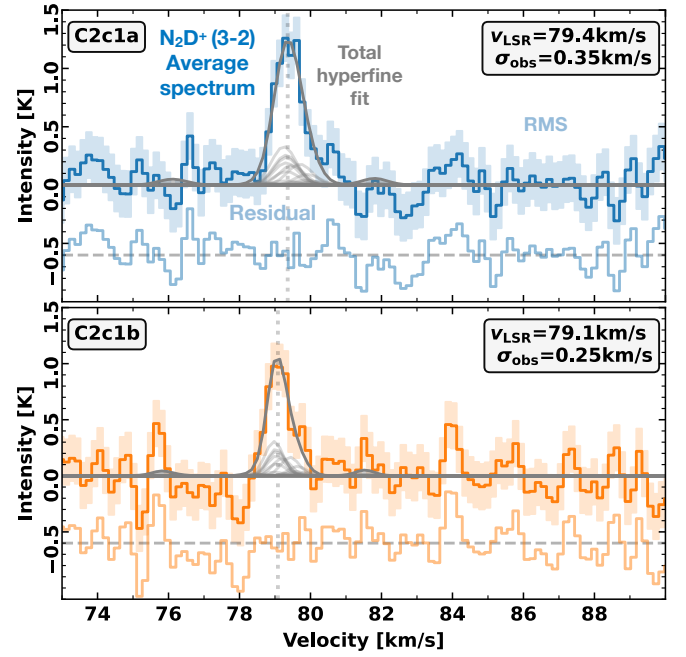


Fig. 2. Spectrum of N_2D^+ (3–2) towards C2c1a (upper panel) and C2c1b (bottom panel). Shown as coloured lines is the spectrum averaged within the boundary of the cores (see Fig. 1), and the coloured shaded regions indicate the uncertainty (rms). Shown in grey is the N_2D^+ (3–2) hyperfine fit to the spectrum assuming optically thin ($\tau = 0.1$) conditions (faded grey curves show the individual hyperfine components of the fit), with the fit parameters shown in the upper right of each panel. The faded spectrum below each profile is the residual of the fit (offset by -0.6 K). Figures A.1 and A.2 show moment and channel maps of the N_2D^+ (3–2) emission across the region, respectively.

$0.6 M_\odot$ for C2c1a and C2c1b. While only representing lower limits for each core, these masses further highlight that even in this lower limit case the core C2c1a contains enough mass to form a high-mass star ($>8 M_\odot$).

4. Gas dynamics of C2c1

We determined the dynamical properties of both cores using this N_2D^+ (3–2) emission (see Appendix A). Figure 2 shows the mean spectra for both cores, which have been extracted within the boundary defined by the dendrogram leaf contours. We fit the spectra with the full hyperfine structure of the N_2D^+ (3–2) line assuming optically thin ($\tau = 0.1$) conditions using the PYSPECKIT package (Ginsburg & Mirocha 2011; Ginsburg et al. 2022). We corrected the measured velocity dispersion (σ_{obs}) for the contribution of the velocity resolution (σ_{res}),

$$\sigma_{\text{obs,corr}}^2 = \sigma_{\text{obs}}^2 - \sigma_{\text{res}}^2 = \sigma_{\text{obs}}^2 - \frac{\Delta v_{\text{res}}^2}{8 \ln 2}, \quad (4)$$

where $\Delta v_{\text{res}} \sim 0.16 \text{ km s}^{-1}$ is the velocity resolution of the observations assuming a Gaussian response for the individual channels in the ALMA receiver (see Koch et al. 2018 for effects of differing spectral response functions on the measured velocity dispersion). Given that the line is resolved by a large number of channels ($\sigma_{\text{obs}}^2/\sigma_{\text{res}}^2 \sim 25$), this correction has a minor effect. Using $\sigma_{\text{obs,corr}}$, we determined the contribution of the

non-thermal motions to the velocity dispersion as

$$\sigma_{\text{NT}}^2 = \sigma_{\text{obs,corr}}^2 - \sigma_{\text{T}}^2 = \sigma_{\text{obs,corr}}^2 - \frac{k_{\text{B}}T_{\text{kin}}}{m_{\text{obs}}}, \quad (5)$$

where σ_{NT} is the non-thermal velocity dispersion, σ_{T} is the thermal velocity dispersion of the observed molecule, and m_{obs} is the observed molecular mass (for N_2D^+ , $m_{\text{obs}} = 30 m_{\text{H}}$). The T_{kin} is the kinetic temperature of the gas, which we assume takes the same value as T_{dust} (10.4 K; see Sect. 3), and k_{B} is the Boltzmann constant.

We examined this non-thermal contribution with respect to the sound speed, $c_{\text{s}} = \sqrt{k_{\text{B}}T_{\text{kin}}/m_{\text{H}}\mu_{\text{p}}}$, where μ_{p} is the mean molecular mass (2.37 for molecular gas at the typical interstellar abundance of H, He, and metals). This is referred to as the one-dimensional sonic Mach number,¹ or $\mathcal{M}_{\text{s}} = \sigma_{\text{NT}}/c_{\text{s}}$. We find \mathcal{M}_{s} of 1.8 and 1.2 for C2c1a and C2c1b, highlighting that both cores appear to have either transonic turbulence or ordered global collapse motions.

We also calculated the total velocity dispersion, σ_{tot} , which includes both thermal and non-thermal motions, following Fuller & Myers (1992),

$$\sigma_{\text{tot}}^2 = \sigma_{\text{obs,corr}}^2 + c_{\text{s}}^2 - \sigma_{\text{T}}^2 = \sigma_{\text{obs,corr}}^2 + k_{\text{B}}T_{\text{kin}} \left(\frac{1}{\bar{m}} - \frac{1}{m_{\text{obs}}} \right), \quad (6)$$

where $\bar{m} = m_{\text{H}}\mu_{\text{p}}$. We find σ_{tot} of 0.39 km s^{-1} and 0.31 km s^{-1} for C2c1a and C2c1b, which are used in the following stability analysis (Sects. 5.2 and 5.3).

5. Stability of C2c1

5.1. Thermal support

We determined the so-called Jeans mass, M_{J} , which gives the maximum mass that can be supported by thermal pressure, and the Jeans length, λ_{J} , which gives the minimum scale for fragmentation. The Jeans mass can be given as (Jeans 1902)

$$M_{\text{J}} = \frac{\pi^{5/2}c_{\text{s}}^3}{6G^{3/2}\rho^{1/2}}, \quad (7)$$

where ρ is the volume density of the core, and G is the gravitational constant. We find M_{J} values of 0.05 and $0.13 M_{\odot}$, corresponding to M/M_{J} of ~ 460 and 12 for C2c1a and C2c1b. These ratios of $M/M_{\text{J}} > 1$ show that the cores are unstable to gravitational collapse if not additionally supported. We estimated the corresponding Jeans length using

$$\lambda_{\text{J}} = c_{\text{s}} \left(\frac{\pi}{G\rho} \right)^{1/2}. \quad (8)$$

We find λ_{J} values of 0.0035 and 0.0090 pc for C2c1a and C2c1b (or 733 and 1900 AU). Comparing these values to the projected radius of the cores, we find $(2r_{\text{eff}})/\lambda_{\text{J}}$ of around 8 and 3 , highlighting that these Jeans-unstable cores could then fragment on size scales similar to the current observed core size scales.

¹ Note that here we have determined the sonic Mach number ($\mathcal{M}_{\text{s}} = \sigma_{\text{NT}}/c_{\text{s}}$) using the one-dimensional velocity dispersion (σ_{NT}). However, this value can be converted to the three-dimensional sonic Mach number by accounting for a factor of $3^{0.5}$: $\mathcal{M}_{\text{s,3D}} = 3^{0.5}\mathcal{M}_{\text{s}}$ (e.g. Palau et al. 2015).

5.2. Thermal and turbulent support

We then assessed the balance of the total kinetic energy, E_{kin} , including both the thermal and turbulent pressure support, against the gravitational potential energy, E_{pot} . These energy terms can be equated to produce the commonly used virial parameter α_{vir} (e.g. Bertoldi & McKee 1992). In the idealised case of a spherical core of uniform density supported by only kinetic energy (i.e. no magnetic fields), the virial parameter takes the form

$$\alpha_{\text{vir}} = a \frac{5\sigma_{\text{tot}}^2 r_{\text{eff}}}{GM}, \quad (9)$$

where r_{eff} is the effective radius of the core, M is the (background-subtracted) mass of the core, and σ_{tot} is the line-of-sight velocity dispersion, that is, assuming the dispersion is a result of the thermal and turbulent broadening (α_{vir} does not account for any systematic infall or outflow motions; see e.g. Kauffmann et al. 2013). The factor a , which accounts both for systems with non-homogeneous and non-spherical density distributions and for a wide range of core shapes and density gradients, takes a value of $a = 2 \pm 1$ (see Bertoldi & McKee 1992). We find virial parameters of 0.1 and 0.7 for C2c1a and C2c1b, respectively, which would be indicative of them being bound and unstable to collapse (i.e. $\alpha_{\text{vir}} < 2$).

We also assessed the fragmentation of the cores using the total Jeans mass, $M_{\text{J,tot}}$, which accounts for the contribution of both the thermal and non-thermal velocity dispersion (no infall or outflow motions). This can be calculated by substituting σ_{tot} for c_{s} in Eq. (7) (e.g. Palau et al. 2015). We find $M_{\text{J,tot}}$ of 0.4 and $0.5 M_{\odot}$, or $M/M_{\text{J,tot}}$ of 55 and 3 , for C2c1a and C2c1b. These total Jeans masses are typically factors of a few higher than when only the thermal support (M_{J}) is accounted for (see Sect. 5.1). However, as shown by the virial parameter, values of $M/M_{\text{J,tot}} > 1$ highlight that the cores are still likely to collapse and/or fragment unless even further supported.

5.3. Thermal, turbulent, and magnetic support

We assessed the relative importance of the magnetic field in preventing gravitational collapse. To do so, we calculated the virial parameter that includes the magnetic field contribution (Pillai et al. 2011),

$$\alpha_{\text{B,vir}} = a \frac{5r_{\text{eff}}}{GM} \left(\sigma_{\text{tot}}^2 - \frac{v_{\text{A}}^2}{6} \right), \quad (10)$$

where the Alfvén velocity is $v_{\text{A}} = B(\mu_0\rho)^{-1/2}$, in which B is the magnetic field strength and μ_0 is the permeability of free space (again, no infall or outflow motions are considered in the velocity dispersion)². Here then we ask how much magnetic field pressure is required in addition to turbulence and thermal pressure to support the cores against gravity. To answer this question, we set $a = 2$ and solved Eq. (10) for B for $\alpha_{\text{B,vir}} < 2$ (Sect. 5.2). We find that the magnetic field strengths required for stability are 10.0 mG and 1.0 mG for C2c1a and C2c1b.

We compared these estimates to the Crutcher et al. (2010) relation linking the magnetic field strength (determined from Zeeman splitting) and volume density (also see Liu et al. 2022),

$$B_{\text{med}} \approx \frac{1}{2}B_0 \left(\frac{n(\text{H})}{n_0} \right)^{2/3} \approx \frac{1}{2}B_0 \left(\frac{2n_{\text{H}_2}}{n_0} \right)^{2/3}, \quad (11)$$

² This expression is valid for SI units; in cgs, the permeability of free space is unity and, hence, removed from the expression.

where $B_{\text{med}} = B_{\text{max}}/2$, and for $n(\text{H}) > n_0$, where $n_0 = 300 \text{ cm}^{-3}$, $n(\text{H}) = 2n_{\text{H}_2}$, and $B_0 = 10 \mu\text{G}$. We find B_{med} values of 14.4 mG and 4.3 mG, or B/B_{med} of 0.7 and 0.2, for C2c1a and C2c1b. This shows that the magnetic field required for the additional support against gravitational collapse could then be more than achieved if these cores follow the [Crutcher et al. \(2010\)](#) relation, which is broadly consistent with the typical magnetic field strengths observed within molecular clouds ([Pillai et al. 2015, 2016; Soam et al. 2019; Tang et al. 2019](#)).

Lastly, we compared the measured core properties to predictions of the turbulent core model ([McKee & Tan 2003](#)). The mass-weighted average velocity dispersion of a virialised core, including pressure equilibrium with its surroundings, is given in the fiducial case by ([McKee & Tan 2003; Tan et al. 2013](#))³

$$\sigma_{\text{c,vir}} = 1.09 \left(\frac{\phi_{\text{B}}}{2.8} \right)^{-3/8} \left(\frac{M}{60 M_{\odot}} \right)^{1/4} \left(\frac{\Sigma_{\text{cl}}}{1 \text{ g cm}^{-2}} \right)^{1/4} \text{ km s}^{-1}, \quad (12)$$

where $\phi_{\text{B}} = 1.3 + 1.5 M_{\text{A}}^{-2} = 2.8$ is a dimensionless parameter that accounts for the effects of magnetic fields ($M_{\text{A}} = 3^{0.5} \sigma_{\text{tot}}/v_{\text{A}} = 1$ is the fiducial Alfvén Mach number), and $\Sigma_{\text{cl}} = 0.6 \text{ g cm}^{-2}$ is the mass surface density of the large-scale C2c1 core taken from the ALMA Infrared-Dark Cloud (IRDC) survey (see [Barnes et al. 2021](#)). We find $\sigma_{\text{c,vir}}$ of 0.70 km s^{-1} and 0.35 km s^{-1} for C2c1a and C2c1b, or $R_{\sigma} = \sigma_{\text{tot}}/\sigma_{\text{c,vir}}$ of 0.56 and 0.87. These values of $R_{\sigma} = \sigma_{\text{tot}}/\sigma_{\text{c,vir}} < 1$ obtained with the above fiducial values would suggest that the core is in a sub-virial state, and on the verge of undergoing collapse because of the lack of sufficient internal pressure support. However, if magnetic fields play a more important role, then this is represented by a smaller Alfvén Mach number (i.e. sub-Alfvén turbulence) and a larger value of ϕ_{B} . For example, using the previously estimated values of B_{med} gives $\sigma_{\text{c,vir}}(B_{\text{med}})$ of 0.26 km s^{-1} and 0.14 km s^{-1} , and $\sigma_{\text{tot}}/\sigma_{\text{c,vir}}(B_{\text{med}})$ of 1.5 and 2.3, which would imply that the cores are close to virial equilibrium and are contracting relatively slowly compared to free-fall collapse.

6. Pre-stellar versus protostellar

The next step is then to determine whether the cores are truly quiescent or show signs of active star formation, which is a key factor in distinguishing between the theories of massive star formation (Sect. 1).

Infrared emission could highlight any embedded protostars within IRDCs, due to the heated dust emission, polycyclic aromatic hydrocarbon emission, or molecular line emission (e.g. [Chambers et al. 2009](#)). We checked *Spitzer* (e.g. 3.6–8 μm , and 24 μm ; [Churchwell et al. 2009; Carey et al. 2009](#)) and *Herschel* (70 μm , [Molinari et al. 2010](#)) data, and confirmed that there are no infrared point sources within any of the bands towards the position of the C2c1 core. The completeness of these surveys at the cloud distance is approximately a few solar masses, depending on the evolutionary stage of the young stellar object (see efforts to classify young stellar objects in similar IRDCs, e.g. [Nguyen Luong et al. 2011](#)). The lack of infrared emission is consistent with them being cold, dense, and quiescent.

In addition, we checked centimetre-radio observations from the THOR project ([Beuther et al. 2016; Wang et al. 2020](#)) and find no significant continuum or radio recombination line emission in the C2 clump region, which would be indicative of a

³ The fiducial case presented here is outlined in Eq. (18) of [McKee & Tan \(2003\)](#), where the fiducial values are taken from their Eq. (12) (also see [Kong et al. 2018; their Eq. \(2\)](#)).

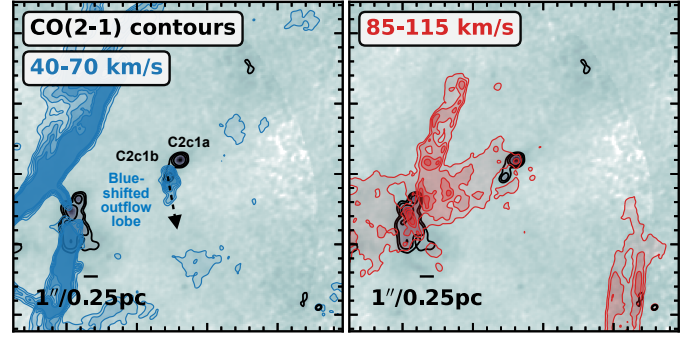


Fig. 3. Evidence for a molecular outflow towards the core. We show in contours the CO (2–1) emission integrated in the ranges 40–70 km s^{-1} (blue contours) and 85–115 km s^{-1} (red contours). The background grey-scale image shown in both panels is the 1 mm continuum emission (see Fig. 1). Highlighted is the associated blueshifted outflow lobe (no redshifted lobe is obvious due to line-of-sight contamination at higher velocities). Shown in the bottom right is the beam size of the observations. Figure B.1 shows channel maps of the CO emission across the region.

lack of embedded H II regions (i.e. from free-free emission). The integrated continuum flux density within a beam-sized aperture (25'') towards the core C2c1 at 1.42 GHz is $\sim 10 \text{ mJy}$ (calculated using the THOR-VLA data combined with the Green Bank Telescope (GBT). More recently, [Wang et al. \(in prep.\)](#) observed this region with higher-resolution and higher-sensitivity MeerKAT L-band observations. The 1.4 GHz continuum image has a resolution of about 6.5 arcsec and rms 65 $\mu\text{Jy/beam}$, and no compact radio sources are seen in the clump. For a box encompassing the starless core, the maximum detected flux is 6 mJy, in broad agreement with the VLA observations. Using the conversion from [Mezger & Henderson \(1967\)](#), these values give a Lyman-continuum photon rate of $\sim 10^{46} \text{ s}^{-1}$, which, based on the stellar models from [Smith et al. \(2002\)](#), gives a zero-age main sequence spectral type of at most B1.5. Hence, we can rule out the presence of any O-type or early B-type stars towards this region.

Moreover, assuming thermal equilibrium between gas and dust, [Wang et al. \(2012\)](#) used the measured temperature of the C2c1 core ($\sim 10 \text{ K}$) to estimate that an at most $\sim 1 L_{\odot}$ protostar could be present within the core. In addition, [Wang et al. \(2012\)](#) observed H₂O and CH₃OH masers with VLA and found a few in the clump, but not near the C2c1 core. All this together again rules out the presence of any significant evolved star formation.

Several works have, however, noted the presence of a weak molecular outflow towards the region (e.g. [Wang et al. 2011; Kong et al. 2019](#)). We investigated this using new higher-sensitivity CO (2–1) observations at an angular resolution of $\sim 0.3''$ (see Fig. 3) – almost an order of magnitude higher resolution than previous studies. We find a weak outflow signature between 40 km s^{-1} and 70 km s^{-1} , which appears to be reminiscent of a single outflow lobe associated with the core that is blueshifted with respect to the systemic velocity (as seen in N₂D⁺; $\sim 80 \text{ km s}^{-1}$). [Wang et al. \(2011\)](#) also determined that C2c1 is driving a weak outflow with a redshifted lobe between 86 and 91 km s^{-1} , as seen in CO (3–2) emission. The identification of such a component is complicated in the higher-resolution CO (2–1) data presented in this work due to the presence of unassociated emission along the line of sight at these higher velocities and imaging artefacts (between 85 and 95 km s^{-1} ; see Fig. B.1). [Wang et al. \(2011\)](#) estimate that this core has the smallest mass outflow rate in the region ($0.73 \times 10^{-5} M_{\odot} \text{ yr}^{-1}$). It is also worth

Table 2. Summary of lines detected towards the cores (see Fig. 4).

Line	Transition	ν (MHz)	T_{up} (K)
H ₂ CS	3(0,3)–2(0,2)	103 040	9.9
H ₂ CS	3(1,2)–2(1,1)	104 617	23.2
DCO ⁺	$J = 3-2 \ v=0$	216 112	20.7
c-HCCCH	3(3,0)–2(2,1) $v=0$	216 278	19.5
CH ₃ CHO	11(1,10)–10(1,9) E $v_t=0$	216 581	64.9
CH ₃ CHO	11(1,10)–10(1,9) A – $v_t=0$	216 630	64.8
H ₂ S	2(2,0)–2(1,1)	216 710	84.0
CH ₃ OH	5(1,4)–4(2,2)	216 945	55.9
SiO	5–4 $v_t=0$	217 104	31.3
DCN	$J = 3-2 \ v=0$	217 238	20.9
c-HCCCH	6(1,6)–5(0,5) $v=0$	217 822	38.6
c-HCCCH	5(1,4)–4(2,3) $v=0$	217 940	35.4
H ₂ CO	3(2,1)–2(0,2)	218 222	21.0
HC ₃ N	$J = 24-23 \ v=0$	218 324	131.0
CH ₃ OH	4(2,2)–3(1,2) $v_t=0$	218 440	45.5
H ₂ CO	3(2,2)–2(2,1)	218 475	68.1
H ₂ CO	3(2,1)–2(2,0)	218 760	68.1
OCS	18–17 $v=0$	218 903	99.8

Notes. We tabulate the line species, transition, rest frequency, and upper energy level, which are taken from the Splatalogue database (Remijan et al. 2007).

highlighting that no associated SiO outflow has been identified towards this region (Liu et al. 2021). Therefore, the outflow is then comparatively weak, which could be indicative of its relative youth. Interestingly, our higher-resolution images show that the outflow begins at the position of the C2c1b core, and that the orientation does not clearly connect to the C2c1a core (see Appendix B for more detail channel maps of the CO emission). These new data could suggest that this outflow is not related to the C2c1a core (as previously suggested), but rather to the C2c1b core. This is an important distinction because in this case, despite its significant mass, C2c1a would remain completely devoid of any active star formation.

7. Chemistry

Chemistry can also be used as an informative proxy for the evolutionary state of a star-forming region. For example, the number of detected lines and their relative strengths can be used to differentiate the pre-stellar or protostellar nature of dense cores (e.g. Nony et al. 2018). To investigate this we show the average broadband spectrum across the C2c1 region in Fig. 4 (blue). In Fig. 4, the 3 mm (102.55–104.35 GHz and 104.55–104.35 GHz) data are taken from the ALMA-IRDC survey (Barnes et al. 2021), and the 1 mm data (215.45–217.35 GHz, 217.55–219.35 GHz, and 232.55–234.35 GHz) are those presented in this work (see Sect. 2). We see that the C2c1 region contains only a limited number of weak lines, which we identified using the CASAVIEWER tool (making use of the Splatalogue database; Remijan et al. 2007). The detected molecules in emission include DCO⁺ and DNC, which are indicative of the core’s early evolutionary stage, as well as H₂CS, H₂CO, and CH₃OH with $T_{\text{up}} = 20\text{--}50$ K, which indicates relatively cold temperatures (see Table 2). In Fig. 4, we compare these results to a more actively star-forming core within the region (C2C5; see Barnes et al. 2021). We see that lines within C2c1 are both systematically weaker and fewer in number compared to C2C5 (also see

Zhang et al. 2015). Indeed, C2C5 has a spectrum more comparable to that of hot core candidates (see Herbst & van Dishoeck 2009). Of particular note is the strong absorption feature seen in SiO (5–4) towards C2c1 that is clearly seen in emission towards C2C5. This is a strong differentiator for the star formation activity of the two cores and further indicates that C2c1 is young, a conclusion that is also in agreement with the lack of SiO outflows previously found in the region.

8. Discussion and summary

Our analysis shows that the C2 core is a very interesting region in the context of massive star formation. We find that at the end of the chain of roughly equally spaced actively star-forming cores (~ 0.15 pc; Zhang et al. 2009; Wang et al. 2011) sits another massive, yet relatively quiescent, core – C2c1. This indicates a potential role for filamentary clouds (see e.g. Jiménez-Serra et al. 2014; Henshaw et al. 2013, 2014; Barnes et al. 2018) in regulating the birth of massive pre-stellar cores.

High-angular-resolution (0.2'' or 0.05 pc) dust continuum observations show that this region fragments into two cores, C2c1a and C2c1b, which have considerable masses of $23 M_{\odot}$ and $2 M_{\odot}$, respectively. Our stability analysis shows that both cores are highly unstable to gravitational collapse (α_{vir} of 0.1 and 0.7) unless supported by magnetic fields of around 1 to 10 mG in strength. These values are high but broadly consistent with the typical magnetic field strengths observed within dense molecular clouds (Pillai et al. 2015, 2016; Soam et al. 2019; Tang et al. 2019). Lastly, we find that there is a weak CO outflow that appears to be associated with C2c1b only. The more massive core, C2c1a, remains completely devoid of any star formation signatures and does not appear to be coincident with the chemistry observed towards more evolved hot cores. Overall, we find that both cores are good targets for studying the early stages of massive star formation. They also offer an interesting comparison to other massive core candidates (e.g. Bontemps et al. 2010; Duarte-Cabral et al. 2013; Wang et al. 2014; Cyganowski et al. 2014; Sanhueza et al. 2017; Nony et al. 2018; Louvet et al. 2019), particularly when focusing on core candidates identified within Cloud C that have been analysed with methods similar to those used in this work (Tan et al. 2013, 2016; Kong et al. 2018).

Tan et al. (2013) used early (cycle 0) ALMA observations of N₂D⁺(3–2) towards IRDCs to identify the C1-S and C1-N cores as candidate massive pre-stellar cores, with masses of $16_{-7}^{+34} M_{\odot}$ and $63_{-27}^{+130} M_{\odot}$, respectively, based on their 1.3 mm dust continuum emission. Following up from this, Tan et al. (2016) and Kong et al. (2018) presented higher-resolution observations of the C1-S region, identifying two early stage protostellar cores in the vicinity; however, the main C1-S starless core was resolved as a distinct spatial and kinematic feature in its N₂D⁺ emission and with a millimetre-continuum derived mass of $59_{-27}^{+123} M_{\odot}$ within a radius of 0.045 pc. Their dynamical analysis of the cores based on the velocity dispersion measured via N₂D⁺(3–2) found moderately sub-virial conditions, and $R_{\sigma} = 0.61_{-0.44}^{+0.88}$ for C1-N and $0.34_{-0.27}^{+0.46}$ for C1-S; the corresponding virial parameters are $\alpha_{\text{vir}} = 0.98_{-0.42}^{+2.4}$ and $0.068_{-0.03}^{+0.15}$, respectively. These values are similar to those calculated for C2c1a and C2c1b (0.56 and 0.87, respectively), also suggesting that they are on the verge of collapse (Sect. 5.3).

In addition, Kong et al. (2017) surveyed 32 IRDC regions and identified N₂D⁺(3–2) cores with the same method. The most massive core in this sample, C9A, has a mass of $M_{\text{c,mm}} = 69.7_{-31.7}^{+146} M_{\odot}$ and $R_{\sigma} = 0.71_{-0.59}^{+0.89}$, while the next most massive

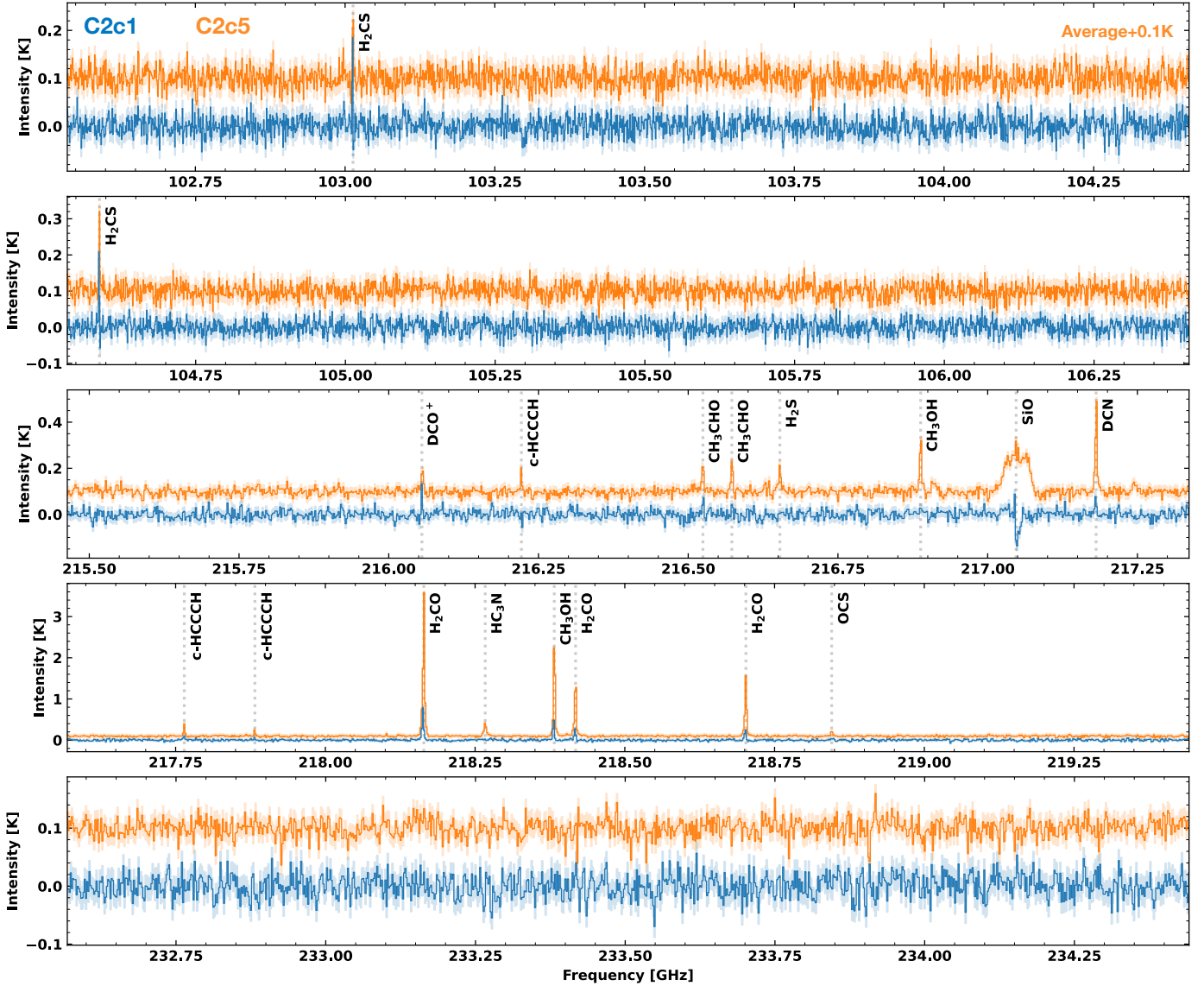


Fig. 4. Spectrum taken across the 3 mm (Barnes et al. 2021) and 1 mm spectral windows towards the C2c1 (blue) and C2c5 (orange) cores. Shown as coloured lines is the spectrum averaged within the boundary of the cores, and the coloured shaded regions indicate the uncertainty (rms). The spectrum of the C2c5 core has been offset by +0.1K to allow comparison. Several prominent lines within the spectral windows, which are summarised in Table 2, are labelled.

is B1A, with $M_{c,mm} = 4.9_{-2.2}^{+10.3} M_{\odot}$ and $R_{\sigma} = 0.85$, again similar to C2c1a and C2c1b. Despite these being particularly promising candidates for massive pre-stellar cores, their analysis is complicated by their proximity, at least in projection, to protostellar sources (Kong et al. 2018).

In combination with the above studies, our results indicate that Cloud C is a particularly rich candidate for studying the early stages of massive star formation. In particular, we find that one core, C2c1a, remains massive enough to form a high-mass star at a radius of around 0.01 pc (or ~ 2000 AU) and yet still appears to be in a pre-stellar evolutionary phase. Such an object could be reminiscent of a massive starless (monolithic) core. The definitive identification of such cores has proven elusive, making C2c1a an exciting prospect for further studies.

Acknowledgements. We are grateful to the anonymous referee for their constructive and detailed suggestions, which helped significantly improve the quality of this paper. We would like Henrik Beuther for their insightful discussions and comments on the draft. A.T.B. and F.B. would like to acknowledge

funding from the European Research Council (ERC) under the European Union’s Horizon 2020 research and innovation programme (grant agreement no. 726384/Empire). J.D.H gratefully acknowledges financial support from the Royal Society (University Research Fellowship) J.C.T. acknowledges support from ERC Advanced Grant MSTAR and NSF grant AST-2009674. K.W. acknowledges support from the National Science Foundation of China (11973013), China Manned Space Project (CMS-CSST-2021-A09), National Key R&D Program of China (2022YFA1603102). This paper makes use of the following ALMA data: ADS/JAO.ALMA#2017.1.00793.S. ALMA is a partnership of ESO (representing its member states), NSF (USA) and NINS (Japan), together with NRC (Canada), MOST and ASIAA (Taiwan), and KASI (Republic of Korea), in cooperation with the Republic of Chile. The Joint ALMA Observatory is operated by ESO, AUI/NRAO and NAOJ.

References

- Barnes, A. T., Kong, S., Tan, J. C., et al. 2016, *MNRAS*, 458, 1990
 Barnes, A. T., Henshaw, J. D., Caselli, P., et al. 2018, *MNRAS*, 475, 5268
 Barnes, A. T., Henshaw, J. D., Fontani, F., et al. 2021, *MNRAS*, 503, 4601
 Bertoldi, F., & McKee, C. F. 1992, *ApJ*, 395, 140
 Beuther, H., Bihl, S., Rugel, M., et al. 2016, *A&A*, 595, A32

- Bonnell, I., Bate, M., Clarke, C., & Pringle, J. 2001, *MNRAS*, **323**, 785
- Bontemps, S., Motte, F., Csengeri, T., & Schneider, N. 2010, *A&A*, **524**, A18
- Butler, M. J., & Tan, J. C. 2009, *ApJ*, **696**, 484
- Carey, S. J., Noriega-Crespo, A., Mizuno, D. R., et al. 2009, *PASP*, **121**, 76
- Chambers, E. T., Jackson, J. M., Rathborne, J. M., & Simon, R. 2009, *ApJS*, **181**, 360
- Churchwell, E., Babler, B. L., Meade, M. R., et al. 2009, *PASP*, **121**, 213
- Crutcher, R. M., Wandelt, B., Heiles, C., Falgarone, E., & Troland, T. H. 2010, *ApJ*, **725**, 466
- Cyganowski, C. J., Brogan, C. L., Hunter, T. R., et al. 2014, *ApJ*, **796**, L2
- Draine, B. T. 2011, *Physics of the Interstellar and Intergalactic Medium* (Princeton University Press)
- Duarte-Cabral, A., Bontemps, S., Motte, F., et al. 2013, *A&A*, **558**, A125
- Fontani, F., Barnes, A. T., Caselli, P., et al. 2021, *MNRAS*, **503**, 4320
- Fuller, G. A., & Myers, P. C. 1992, *ApJ*, **384**, 523
- Ginsburg, A., & Mirocha, J. 2011, Astrophysics Source Code Library, [record [ascl:1109.001](https://ui.adsabs.org/abs/2011ascl...1109...001)]
- Ginsburg, A., Sokolov, V., de Val-Borro, M., et al. 2022, *AJ*, **163**, 291
- Henshaw, J. D., Caselli, P., Fontani, F., et al. 2013, *MNRAS*, **428**, 3425
- Henshaw, J. D., Caselli, P., Fontani, F., Jiménez-Serra, I., & Tan, J. C. 2014, *MNRAS*, **440**, 2860
- Henshaw, J. D., Caselli, P., Fontani, F., et al. 2016, *MNRAS*, **463**, 146
- Henshaw, J. D., Jiménez-Serra, I., Longmore, S. N., et al. 2017, *MNRAS*, **464**, L31
- Herbst, E., & van Dishoeck, E. F. 2009, *ARA&A*, **47**, 427
- Jean, J. H. 1902, *Philos. Trans. Roy. Soc. Lond. Ser. A*, **199**, 1
- Jiménez-Serra, I., Caselli, P., Fontani, F., et al. 2014, *MNRAS*, **439**, 1996
- Kainulainen, J., & Tan, J. C. 2013, *A&A*, **549**, A53
- Kauffmann, J., Pillai, T., & Zhang, Q. 2013, *ApJ*, **765**, L35
- Koch, E., Rosolowsky, E., & Leroy, A. K. 2018, *RNAAS*, **2**, 220
- Kong, S., Tan, J. C., Caselli, P., et al. 2016, *ApJ*, **821**, 94
- Kong, S., Tan, J. C., Caselli, P., et al. 2017, *ApJ*, **834**, 193
- Kong, S., Tan, J. C., Caselli, P., et al. 2018, *ApJ*, **867**, 94
- Kong, S., Arce, H. G., Maureira, M. J., et al. 2019, *ApJ*, **874**, 104
- Krumholz, M. R., Bate, M. R., Arce, H. G., et al. 2014, in *Protostars and Planets VI*, eds. H. Beuther, R. S. Klessen, C. P. Dullemond, & T. Henning, 243
- Liu, J., Zhang, Q., Qiu, K., et al. 2020, *ApJ*, **895**, 142
- Liu, J., Qiu, K., & Zhang, Q. 2022, *ApJ*, **925**, 30
- Liu, M., Tan, J. C., Cheng, Y., & Kong, S. 2018, *ApJ*, **862**, 105
- Liu, M., Tan, J. C., Marvil, J., et al. 2021, *ApJ*, **921**, 96
- Louvet, F., Neupane, S., Garay, G., et al. 2019, *A&A*, **622**, A99
- Mathis, J. S., Rumpl, W., & Nordsieck, K. H. 1977, *ApJ*, **217**, 425
- McKee, C. F., & Tan, J. C. 2003, *ApJ*, **585**, 850
- McLaughlin, D. E., & Pudritz, R. E. 1997, *ApJ*, **476**, 750
- Mezger, P. G., & Henderson, A. P. 1967, *ApJ*, **147**, 471
- Molinari, S., Swinyard, B., Bally, J., et al. 2010, *PASP*, **122**, 314
- Myers, P. C. 2009, *ApJ*, **700**, 1609
- Nguyen Luong, Q., Motte, F., Hennemann, M., et al. 2011, *A&A*, **535**, A76
- Nony, T., Louvet, F., Motte, F., et al. 2018, *A&A*, **618**, A5
- Ossenkopf, V., & Henning, T. 1994, *A&A*, **291**, 943
- Padoan, P., Pan, L., Juvela, M., Haugbølle, T., & Nordlund, Å. 2020, *ApJ*, **900**, 82
- Palau, A., Ballesteros-Paredes, J., Vázquez-Semadeni, E., et al. 2015, *MNRAS*, **453**, 3785
- Pillai, T., Kauffmann, J., Wyrowski, F., et al. 2011, *A&A*, **530**, A118
- Pillai, T., Kauffmann, J., Tan, J. C., et al. 2015, *ApJ*, **799**, 74
- Pillai, T., Kauffmann, J., Wiesemeyer, H., & Menten, K. M. 2016, *A&A*, **591**, A19
- Remijan, A. J., Markwick-Kemper, A., & ALMA Working Group on Spectral Line Frequencies 2007, in *American Astronomical Society Meeting Abstracts*, **211**, 132.11
- Rosolowsky, E. W., Pineda, J. E., Kauffmann, J., & Goodman, A. A. 2008, *ApJ*, **679**, 1338
- Sanhueza, P., Jackson, J. M., Zhang, Q., et al. 2017, *ApJ*, **841**, 97
- Simon, R., Rathborne, J. M., Shah, R. Y., Jackson, J. M., & Chambers, E. T. 2006, *ApJ*, **653**, 1325
- Smith, L. J., Norris, R. P. F., & Crowther, P. A. 2002, *MNRAS*, **337**, 1309
- Soam, A., Liu, T., Andersson, B. G., et al. 2019, *ApJ*, **883**, 95
- Tan, J. C., Kong, S., Butler, M. J., Caselli, P., & Fontani, F. 2013, *ApJ*, **779**, 96
- Tan, J. C., Beltrán, M. T., Caselli, P., et al. 2014, *Protostars and Planets VI*, 149
- Tan, J. C., Kong, S., Zhang, Y., et al. 2016, *ApJ*, **821**, L3
- Tang, Y.-W., Koch, P. M., Peretto, N., et al. 2019, *ApJ*, **878**, 10
- Wang, K. 2015, *The Earliest Stages of Massive Clustered Star Formation: Fragmentation of Infrared Dark Clouds* (Berlin, Heidelberg: Springer-Verlag)
- Wang, Y., Zhang, Q., Pillai, T., Wyrowski, F., & Wu, Y. 2008, *ApJ*, **672**, L33
- Wang, P., Li, Z.-Y., Abel, T., & Nakamura, F. 2010, *ApJ*, **709**, 27
- Wang, K., Zhang, Q., Wu, Y., & Zhang, H. 2011, *ApJ*, **735**, 64
- Wang, K., Zhang, Q., Wu, Y., Li, H.-b., & Zhang, H. 2012, *ApJ*, **745**, L30
- Wang, K., Zhang, Q., Testi, L., et al. 2014, *MNRAS*, **439**, 3275
- Wang, Y., Beuther, H., Rugel, M. R., et al. 2020, *A&A*, **634**, A83
- Zhang, Q., Wang, K., Lu, X., & Jiménez-Serra, I. 2015, *ApJ*, **804**, 141
- Zhang, Q., Wang, Y., Pillai, T., & Rathborne, J. 2009, *ApJ*, **696**, 268

Appendix A: Integrated intensity maps of N_2D^+

In Fig. A.1, we show moment maps (integrated intensity, max intensity, intensity-weighted centroid velocity, and intensity-weighted velocity dispersion) of the N_2D^+ (3-2) emission. We see that the N_2D^+ emission is widespread across both cores as seen in the dust continuum, even bridging the region between the cores. This indicates that the gas surrounding the cores is also cold and could contribute to accretion. We also see that there is a velocity gradient across the core region, from low velocities at C2c1b to high velocities at C2c1a, which could indicate that

the system is rotating. This velocity gradient can also be seen in the channel maps presented in Fig. A.2, which shows the N_2D^+ emission integrated in velocity bins of 0.5 km s^{-1} . Interestingly, we see that there is an emission feature that extends to the north of the system in the velocity bins of $80.5 - 81.5 \text{ km s}^{-1}$, which can also be seen as a sharp cut in the velocity field map (Fig. A.1). If this emission is connected to the core, this could suggest that dense molecular gas is still being accreted onto the core envelope. An in-depth analysis of inflow and the accretion signature will be performed in a future work.

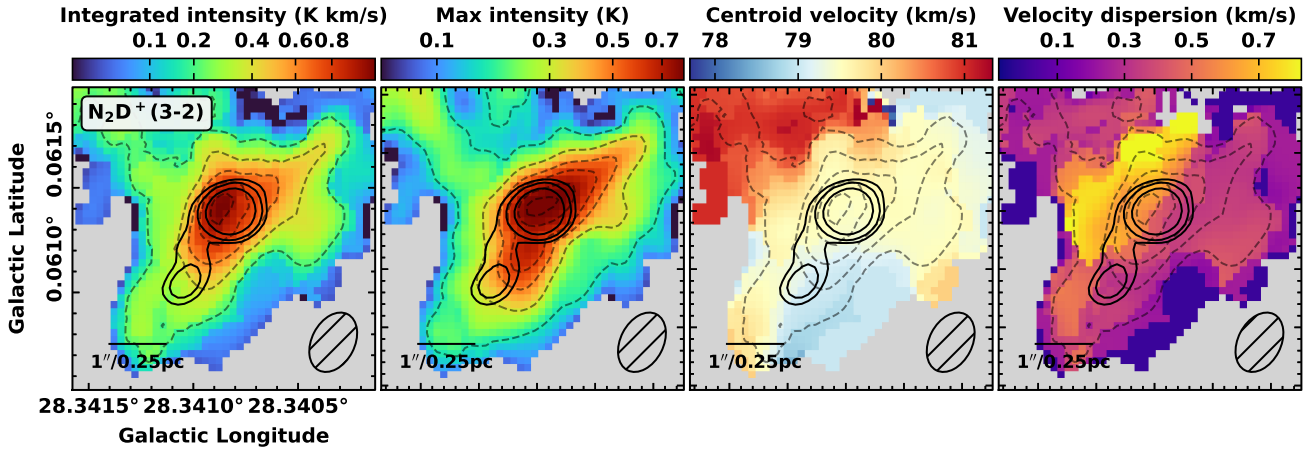


Fig. A.1. Distribution of N_2D^+ (3-2) emission across the core C2c1 region. (panels from left to right) Integrated intensity, peak intensity, intensity-weighted centroid velocity, and intensity-weighted velocity dispersion. Overlaid as solid black contours is the ALMA 1 mm dust continuum at $0.3''$ resolution (see Fig. 1). The dashed contours in the first, third, and fourth panels are the integrated intensity, and in the second panel they are the maximum intensity. Shown on the right of the panels is the beam size, and a scale bar is shown in the lower left of all panels.

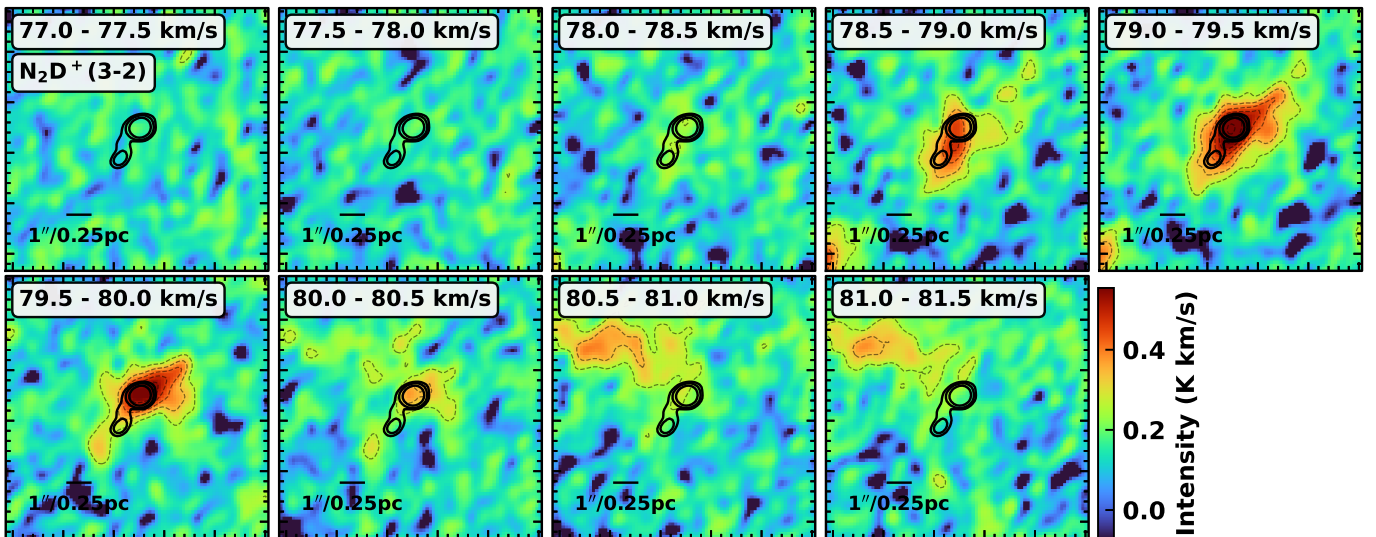


Fig. A.2. Channel maps of the N_2D^+ (3-2) emission across the core region. Overlaid as contours is the ALMA 1 mm dust continuum at $0.3''$ resolution (see Fig. 1). A scale bar is shown in the lower left of all panels.

Appendix B: Outflows

In Fig. B.1 we show the CO (2-1) emission integrated in velocity bins of 2.5 km s^{-1} from 40 km s^{-1} to 112.5 km s^{-1} . The outflow feature can be seen towards core C2c1b between velocities of 55 km s^{-1} and 77.5 km s^{-1} . We do not find a similar feature at higher velocities that extends across such a large velocity range ($\sim 20 \text{ km s}^{-1}$). Indeed, the identification of a redshifted

counterpart to this outflow (e.g. from around 70 km s^{-1} to 90 km s^{-1}) is complicated by the presence of imaging artefacts. That said, there is some emission in the direction where the redshifted lobe would be expected within the 75 km s^{-1} to 77.5 km s^{-1} channel. Yet, it is not clear if it is associated with the extended emission along the line of sight that can also be seen at higher velocities (85 km s^{-1} to 92.5 km s^{-1}).

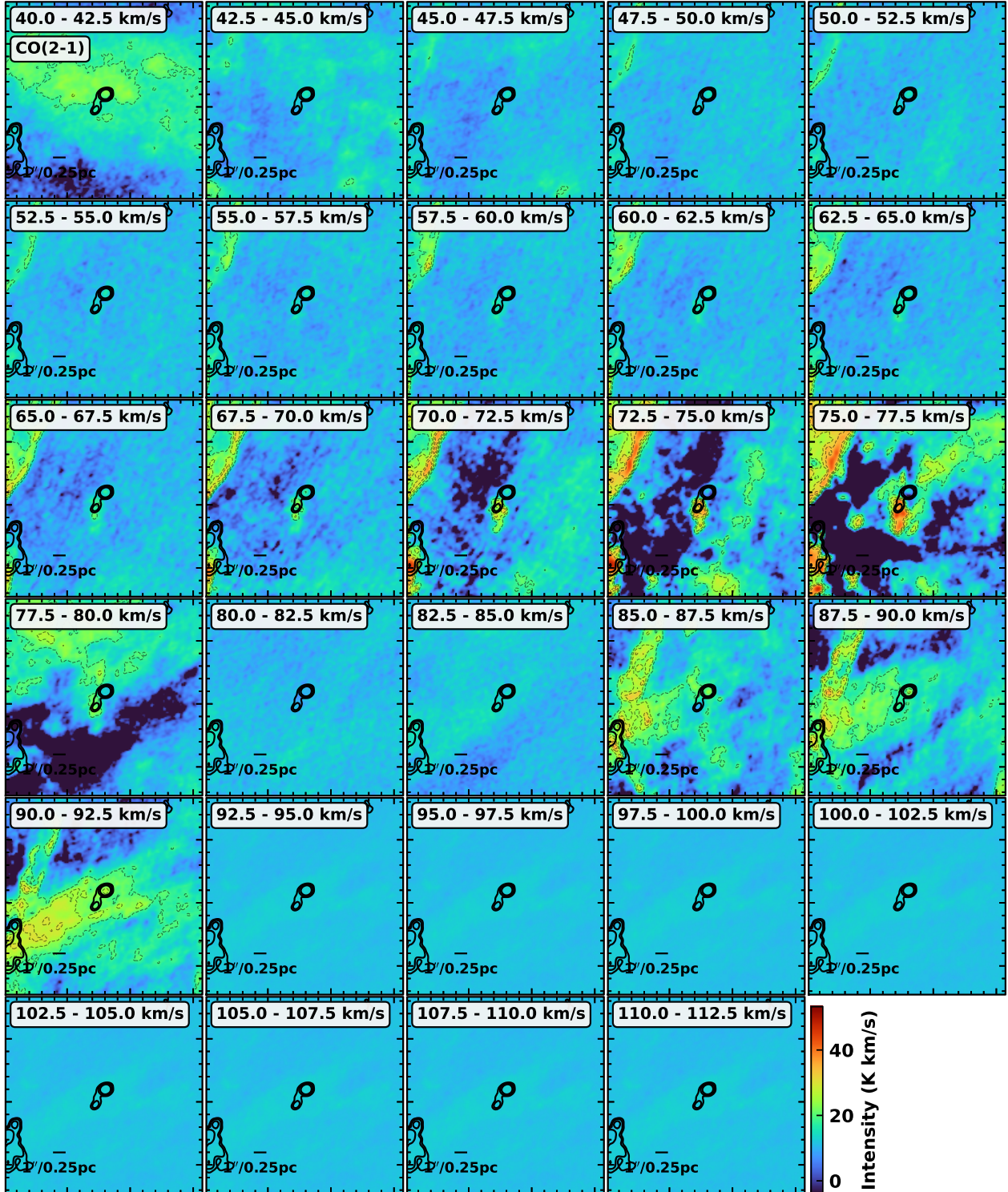


Fig. B.1. Channel maps of the CO (2-1) emission across the core region. Overlaid as contours are the ALMA 1 mm dust continuum at $0.3''$ resolution (see Fig. 1). A scale bar is shown in the lower left of all panels.